Journal of Solid Mechanics Vol. 11, No. 4 (2019) pp. 825-841
DOI: 10.22034/jsm.2019.668616

The Effects of Forming Parameters on the Single Point Incremental Forming of 1050 Aluminum Alloy Sheet

R. Safdarian *

Department of Mechanical Engineering, Behbahan Khatam Alanbia University of Technology, Behbahan, Iran

Received 26 July 2019; accepted 28 September 2019

ABSTRACT

The single point incremental forming (SPIF) is one of the dieless forming processes which is widely used in the sheet metal forming. The correct selection of the SPIF parameters influences the formability and quality of the product. In the present study, the Gurson-Tvergaard Needleman (GTN) damage model was used for the fracture prediction in the numerical simulation of the SPIF process of aluminum alloy 1050. The GTN parameters of AA 1050 sheet were firstly identified by the numerical simulation of tensile test and comparison of the experimental and numerical stress-strain curves. The identified parameters of the GTN damage model were used for fracture prediction in the SPIF process. The numerical results of the fracture position, thickness variation across the sample and forming height were compared with the experimental results. The numerical results had good agreement with the experimental ones. The effect of SPIF main parameters was investigated on the formability of samples by the verified numerical model. These parameters were tool rotation speed, tool feed rate, tool diameter, wall angle of the sample, vertical pitch, and friction between the tool and the blank.

Keywords: Single point incremental forming (SPIF); GTN damage model; Response surface method (RSM); Fracture; Finite element method (FEM).

1 INTRODUCTION

SINGLE point incremental forming (SPIF) process is one of the dieless sheet metal forming processes are widely studied in the research papers. Because of the capability of the SPIF process to complex shape manufacturing, this process can be widely used in the automotive and aerospace industries. Bagudanch et al. [1] studied the effect of the variation of several process parameters in the SPIF. Their results showed that spindle speed variation was the most significant parameter. Gatea et al. [2] reviewed some of the studies in the technological

*Corresponding author. Tel.: +98 61 52721191.
E-mail address: safdarian@bkatu.ac.ir (R. Safdarian).

capabilities and limitations of the SPIF. The effect of process parameters was studied on the formability, deformation mechanics and springback. Raju et al. [3] used a SPIF experimental setup for forming of multiple commercially pure aluminum sheets. Their results showed that the sheets failed under the combination of shear and brittle failure mode. Guzmán et al. [4] used an extended Gurson-Tvergaard-Needleman (GTN) model and finite element (FE) simulation to predict damage in the SPIF. Their results showed that wrong coalescence modeling in the GTN model caused the underestimates of failure angle in the SPIF. Dakhli et al. [5] used the experimental tests of SPIF for forming two geometries of parts with the same process parameters. They studied the effects of straight and circular generatrix profiles on the forming forces, thickness distribution, shape accuracy and surface roughness of the formed shape. Their results indicated that using straight generatrix caused a more uniform thickness distribution in the final part. McAnulty et al. [6] reviewed 35 papers in the field of SPIF and the effect of process parameters on the formability of the sheet in this process. Results of this study showed that there is a lack of focus on the parameter interactions in the literature. Bagudanch et al. [7] studied the forming forces in the SPIF of variable wall angle geometry under different bending conditions. Their results indicated that the maximum forming force decreased by the spindle speed increase while it was increased by the tool diameter increase. The effect of temperature and tool rotation speed was studied on the SPIF of titanium alloy by Palumbo and Brandizzi [8]. The effect of heating by an electrical heater and high tool rotation speed were studied on the formability of Ti6Al4V blank. Their results indicated that high rotation speed had a positive effect on the formability and increased the level of stretching. Hadoush and van den Boogaard [9] used a substructuring method for time reduction of implicit simulations of the SPIF. In this method, the finite element mesh was divided into several non-overlapping parts. Their results showed that this method was 2.4 faster than the classical implicit method. Duflou et al. [10] used experimentally multi-step tool path strategy to increase the process window. Their results showed that the formability increased by the multi-step forming. Gupta and Jeswiet [11] studied the effect of feed rate and tool rotation speed on the temperature in the SPIF of AA5754-H32. They founded that lubricant and rig design had an effect on the net heat within the system. Edwards et al. [12] did experimental tests of the SPIF to investigate the effect of forming parameters on the springback of polycarbonate sheets. Results showed that the springback decreased by the spindle rotational speed and the feed rate increase. Bansal et al. [13] used an analytical model to predict the sheet thickness, forming forces and contact area in the SPIF. Predicted results were compared with experimental ones. Results showed that the presented analytical model required less computational resources compared to the FE analysis. Behera et al. [14] reviewed some of studies and developments in the SPIF field. The different aspect of this process like tool path and tooling strategies, failure mechanism, forming mechanics and estimation of forming force were investigated and provided a roadmap for future of this process. Martins et al. [15] presented a theoretical analysis of the SPIF. This theoretical model was based on the membrane analysis with bi-directional in plane contact friction. Martínez-Romero et al. [16] studied the dynamic interaction among the tool, the sheet and the die during the forming process. Their results showed that a robust experimental setup needed to avoid undesirable effects of vibration on the final part.

In the present study, the Gurson-Tvergaard Needleman (GTN) damage model was used for the fracture prediction in the SPIF process of aluminum alloy 1050. Response surface method (RSM) was coupled with the finite element to identify the GTN parameters of the AA 1050 sheet. For this purpose, different sets of the GTN parameters were used for simulation of the uniaxial tensile test in the Abaqus/Explicit. Then, the optimum parameters were selected based on the comparison of the experimental and numerical stress-strain curves. The identified GTN parameters were used in the numerical simulation of the SPIF process of AA 1050 to produce a truncated conical geometry. The numerical model of the SPIF was verified with the experimental tests of the present study. The verified model was used to investigate the effect of the SPIF parameters on the formability, forming height, and thickness variations in the critical element. These forming parameters were: tool diameter, tool rotation speed, tool feed rate, vertical pitch, friction between the tool and the blank and wall angle of the sample. The novelties of the present study are: (1) identification of GTN parameters of AA 1050 sheet using the anti-inference method and numerical simulation of tensile test based on the RSM design of experiment, (2) investigation of effect of GTN parameters on the ultimate stress and related strain in the stress-strain curve of AA 1050 sheet, (3) investigation of effects of main parameters of SPIF on the formability and thinning of AA 1050 sheet using the experimental tests and numerical simulations.

2 METHODOLOGY

2.1 Material properties

In the present study, the 1050 aluminum alloy sheet with 1 *mm* thickness was used in the SPIF process. This aluminum alloy has electrical conductivity, excellent corrosion resistance, and high ductility. Therefore, the AA 1050 is mostly used in the automotive industry, food industry containers, chemical process plant equipment, and light reflectors. The uniaxial tensile test based on the ASTM standard [17] was used to calculate the mechanical properties of this aluminum alloy. Fig. 1 shows the true stress-strain curve of the AA 1050 sheet.

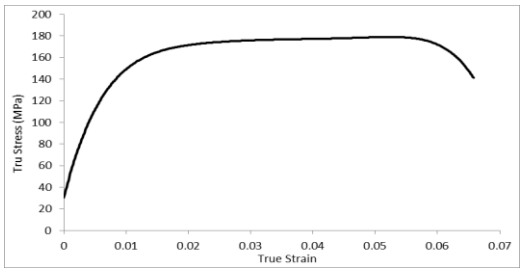

Fig.1
True stress-strain curve of AA 1050.

2.2 The experimental setup of the SPIF

In the present study, the square sheet of AA 1050 with the dimension of 200 *mm*×200*mm* and the thickness of 1 *mm* was used for the SPIF process. As Fig. 2 (a) shows a three-axis CNC milling machine was used for this process and the G-cod of spiral tool paths was generated using the CAM software Power Mill. The blank was fixed from four edges in the fixture to avoid any movement. The forming tool was a cylindrical rod of diameter 14 *mm* with a hemispherical head which was made of high-speed steel (HSS). The designed part for production in the SPIF is a truncated cone with a constant wall angle of 30˚ and depth of 66 *mm*. Fig. 2 (b) shows the designed part in the Solid Works software. Although the depth of the final part is 66 *mm*, it maybe reduces by the forming condition variations such as friction condition between the blank and the forming tool. Two different contact conditions were used between the forming tool and the blank in the experimental tests of the SPIF. In one set of the experimental tests, the hydraulic oil was used as a lubricant in the blank and tool contact and another set of experimental tests were done without lubricant.

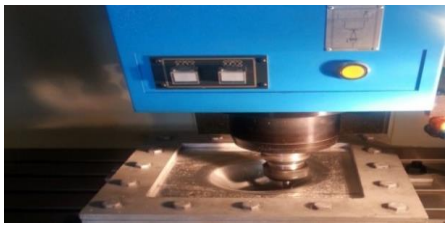

(a)

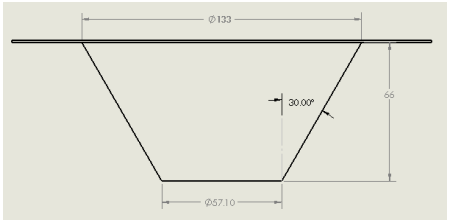

(b)

Fig.2
(a) The experimental setup of the SPIF,. (b) The design truncated cone for experimental and numerical tests.

2.3 Identification of GTN damage parameters

The Gurson–Tvergaard–Needleman (GTN) based on the following equation was used for the fracture prediction in the SPIF of AA 1050 sheet.

$$\varphi = \left(\frac{\sigma_{eq}}{\sigma_y}\right)^2 + 2q_1 f^* .cosh\left(\frac{3q_2\sigma_m}{2\sigma_y}\right) - 1 - q_3 f^{*2} = 0 \qquad (1)$$

where σ_m is the mean stress, σ_{eq} is the Von Mises equivalent stress, σ_y is the yield stress of material, q_1, q_2 and q_3 are tha material parameters.

The relationship between f^* and f is given as follows:

$$f^* = \begin{cases} f & f \leq f_c \\ f_c + \dfrac{1/q_1 - f_c}{f_f - f_c} & f_c \prec f \prec f_f \end{cases} \tag{2}$$

where f_f is void volume fraction at total failure and f_c is critical void volume fraction. f is the void volume fraction which is the ratio of total volume of cavities to the volume of the body. The growth of existing voids and nucleation of new voids cause the increase of total void volume fraction. Therefore, the rate of void volume fraction can be shown by the following equation:

$$\dot{f} = \dot{f}_{growth} + \dot{f}_{nucleation} \tag{3}$$

The plastic incompressibility of a circumambient matrix of the voids based on the mass balance in representative volume elements is used to specify the void growth rate.

$$\dot{f}_{growth} = (1-f).\dot{\varepsilon}_{kk}^{pl} \tag{4}$$

where $\dot{\varepsilon}_{kk}^{pl}$ is the plastic hydrostatic strain.

Normal distribution of void nucleation was proposed by [18] using the following equation:

$$\dot{f}_{nucleation} = A\,\dot{\bar{\varepsilon}}^{pl} = \frac{f_N}{S_N\sqrt{2\pi}} exp\left[-\frac{1}{2}\left(\frac{\bar{\varepsilon}^{pl} - \varepsilon_N}{S_N}\right)^2\right]\dot{\bar{\varepsilon}}^{pl} \tag{5}$$

where S_N is standard deviation, $\bar{\varepsilon}^{pl}$ the equivalent plastic strain of the material, ε_N the mean value of the distribution of plastic strain, f_N the volume fraction of void nucleation.

The coefficients of $f_0, f_c, f_N, f_f, \varepsilon_N, S_N, q_1, q_2$ and q_2 required to be identified for using the GTN damage model. The value of GTN parameters related to the materials microstructure is different for each material. Anti-inference method is one of the methods for calculation of GTN parameters which was used by He et al. [19]. In this method, the combination of the FE simulation with the experimental tensile test is used and the GTN parameter identified by the comparison of the numerical and experimental stress-strain curves. In the present study, the initial values of the GTN parameters for AA 1050 were selected based on the results of Kacem et al. [20]. Table 1., shows the GTN parameters of Kacem et al. [20].

Table 1
Known parameters of GTN model for AA 1050 [20]

Parameter	q_1	q_2	q_3	S_N	f_0	ε_N	f_N	f_f	f_c
Value	1.5	1	2.25	0.1	0	0.3	0.004	032	0.014

For a better selection of the GTN parameters, a design of experiment (DOE) was done using the Response Surface Method (RSM) with the technique of Central Composite Design (CCD) and considering the parameters of Ref. [20]. In this DOE, the maximum numerical stress and numerical strain at the maximum stress of the stress-strain curve were compared with the experimental ones. The value of q_1, q_2, q_3, f_0, and S_N was selected as constant in the numerical simulation using information of Table 1. For other GTN parameters, a range of value was considered based on the results of Kacem et al. [20]. These parameters were mean $0.1 \prec \varepsilon_N \prec 0.4$, effective void volume fraction $0.002 \prec f_N \prec 0.006$, the final void volume fraction $0.2 \prec f_f \prec 0.35$ and critical void volume fraction $0.005 \prec f_c \prec 0.02$. Table 2., shows the list of 31 runs of numerical simulation of tensile test with different parameters for the GTN model. The stress–strain curve of these numerical simulations were compared with the experimental results.

Table 2
The DOE of numerical simulation of the tensile test.

Run num.	ε_N	f_N	f_f	f_c
1	0.25	0.004	0.275	0.0125
2	0.1	0.006	0.2	0.005
3	0.25	0.004	0.275	0.0125
4	0.1	0.002	0.35	0.005
5	0.25	0.005	0.275	0.0125
6	0.25	0.004	0.275	0.01625
7	0.175	0.004	0.275	0.0125
8	0.1	0.006	0.35	0.005
9	0.25	0.004	0.2375	0.0125
10	0.25	0.004	0.275	0.0125
11	0.4	0.002	0.35	0.02
12	0.1	0.002	0.2	0.02
13	0.4	0.006	0.35	0.02
14	0.325	0.004	0.275	0.0125
15	0.25	0.004	0.275	0.0125
16	0.4	0.002	0.2	0.02
17	0.25	0.004	0.3125	0.0125
18	0.4	0.006	0.2	0.02
19	0.1	0.006	0.35	0.02
20	0.25	0.003	0.275	0.0125
21	0.25	0.004	0.275	0.0125
22	0.4	0.006	0.2	0.005
23	0.25	0.004	0.275	0.0125
24	0.4	0.002	0.35	0.005
25	0.25	0.004	0.275	0.0125
26	0.25	0.004	0.275	0.00875
27	0.1	0.006	0.2	0.02
28	0.1	0.002	0.35	0.02
29	0.1	0.002	0.2	0.005
30	0.4	0.002	0.2	0.005
31	0.4	0.006	0.35	0.005
Ref. [20]	0.3	0.004	0.32	0.014

2.4 Numerical simulation

In the first part of the numerical simulation, the uniaxial tensile test was modeled based on the experimental test conditions in the commercially available finite element code Abaqus/Explicit 6.14 to determine the GTN parameters. Because of symmetry, just half of the uniaxial sample was modeled in the Abaqus. The nine parameters of the GTN damage model imported into the material properties of numerical simulation and 32 simulations were done based on Table 2. The void volume fraction (VVF) criterion was used to identify the first damaged element. When the VVF equaled to the f_f , the element started to damage and the stress-strain curve of the damaged element compared with the experimental one. In the second part of the numerical simulation, the process of the SPIF was modeled in the Abaqus/Explicit 6.14. This model consists of the AA 1050 blank and the forming tool. Because of negligible deformation of the forming tool, it was modeled as a rigid body. The AA 1050 blank was modeled as a deformable part by four nodes Kirchhoff thin shell elements (S4R) with shell thickness equal to the thickness of

blank (1 *mm*), five Gaussian integration points through the thickness and dimensions of 200 *mm*×200 *mm*. The blank's edges fixed by using encastre boundary condition. Fig. 3 shows this model, the boundary conditions, and the meshed blank. As this figure shows, the fine mesh was used for the blank. The forming tool is a cylindrical rod with a hemispherical head which touches the blank in the forming process. The tool had rotation speed about its axis and also moved in three directions. As mentioned in the experimental part, the designed geometry for the SPIF was the truncated cone with a constant wall angle (Fig. 2).

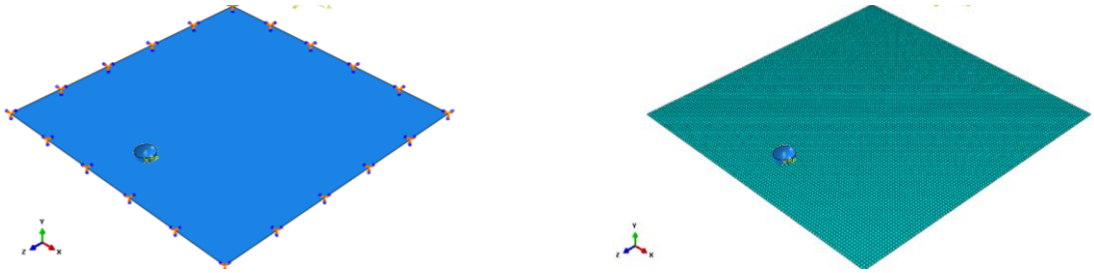

Fig.3
Numerical model for the SPIF process in the Abaqus/Explicit.

The Solidworks software was used to produce the tool path coordinate which was a helix path. These coordinates were imported as boundary conditions of the forming tool to the Abaqus. After verification of the SPIF numerical model with the experimental tests of the present study, this model was used to investigate the effect of forming parameters on the formability and thickness distribution of AA 1050 blank in the SPIF. The GTN damage model whose parameters were identified in the previous section used for fracture prediction in the FE simulation of the SPIF process. The void volume fracture (VVF) criterion was used to predict the position and time of fracture in the blank. When the VVF equals to the f_f , the element starts to damage. The forming parameters and their values have been shown in Table 3.

Table 3
Forming parameters of the SPIF and their values.

Forming parameters	Verification	Level 1	Level 2	Level 3
Tool diameters (*mm*)	14	12	16	18
Tool rotational speed (*rpm*)	250	100	500	1000
Feed rate (*mm/s*)	6500	6500	7500	8000
Helix pitch (*mm*)	0.6	1.2	2	3.5
Wall angle (degree)	30˚	25˚	35˚	45˚
Friction between the tool and sheet	0.4	0.2	0.4	0.8

3 RESULTS

3.1 Identification of GTN parameters

The effect of GTN parameters was studied on the maximum stress and strain at the maximum stress of the stress-strain curve from the tensile test. The VVF criterion was used for selection of the first element of the sample which started to fracture in the Abaqus simulations. The stress-strain curve of the first element which it's VVF = f_f was compared with the experimental one. Table 4., shows the numerical stress, numerical strain, and their error values compared to the experimental results. As Table 4., shows, the error values of the numerical stress for all simulations is less than 1 % and this shows that the maximum stress of numerical stress-strain curve is near to the experimental results and it is not sensitive to the variation of the GTN parameters. This table shows that the numerical strain is more sensitive to the selected GTN parameters than the numerical stress. The effect of GTN parameters on the error value of the numerical strain has been shown in Fig. 4. As this figure shows, the error value decreased by the increase of ε_N and increased by the increase of f_N . The variation of f_f and f_c didn't have a significant influence on the error value of the numerical strain. The minimum error value happened for $\varepsilon_N = 0.4$ and $f_N = 0.002$ which were selected as optimum values for these two parameters of the GTN model. Whereas the variation of two other parameters of f_f and f_c didn't have a significant influence on the error value of the numerical strain, the suggested

values by Kacem et al. [20] were selected as optimum parameters for these parameters. Therefore, the optimum parameters of the GTN damage model for fracture prediction in the SPIF process of AA 1050 have been summarized in Table 5.

Table 4
Comparison of numerical and experimental stress and strain.

Run num.	Numerical strain	Numerical stress	Error value of strain (%)	Error value of stress (%)
1	0.056893	177.297	9.410	0.730
2	0.057973	177.029	11.486	0.880
3	0.056893	177.297	9.410	0.730
4	0.056678	177.217	8.997	0.775
5	0.057079	177.297	9.767	0.730
6	0.056893	177.297	9.410	0.730
7	0.056531	177.221	8.714	0.772
8	0.057973	177.029	11.486	0.880
9	0.056893	177.297	9.410	0.730
10	0.056893	177.297	9.410	0.730
11	0.0564	177.287	8.461	0.735
12	0.056678	177.217	8.997	0.775
13	0.056392	177.287	8.447	0.735
14	0.056466	177.288	8.589	0.735
15	0.056893	177.297	9.410	0.730
16	0.0564	177.287	8.461	0.735
17	0.056893	177.297	9.410	0.730
18	0.056392	177.287	8.447	0.735
19	0.057973	177.029	11.486	0.880
20	0.056801	177.297	9.232	0.730
21	0.056893	177.297	9.410	0.730
22	0.056392	177.287	8.447	0.735
23	0.056893	177.297	9.410	0.730
24	0.0564	177.287	8.461	0.735
25	0.056893	177.297	9.410	0.730
26	0.056893	177.297	9.410	0.730
27	0.057973	177.029	11.486	0.880
28	0.056678	177.217	8.997	0.775
29	0.056678	177.217	8.997	0.775
30	0.0564	177.287	8.461	0.735
31	0.056392	177.287	8.447	0.735
Ref. [20]	0.056577	177.294	8.801	0.731

Table 5
The optimum parameters of the GTN model for AA 1050.

Parameter	q_1	q_2	q_3	S_N	f_0	ε_N	f_N	f_f	f_c
Value	1.5	1	2.25	0.1	0	0.4	0.004	0.320	0.014

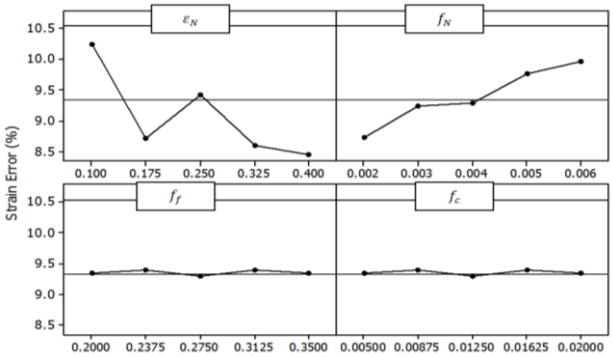

Fig.4
The effect of GTN parameters on the error value of numerical strain.

3.2 Fracture prediction of the SPIF process by the GTN model

For verification of the SPIF numerical model, some experimental tests were done using the forming parameters of Table 3., (verification column). These experimental tests were done in two different contact conditions between the tool and the blank. Because of using oil as a lubricant in the blank and tool contact, one set of the experimental tests was done in the frictionless condition. The second set of experimental tests of the SPIF was done without any lubricant between the tool and the blank. The numerical simulations of the SPIF were done in the conditions of the experimental tests. The GTN damage model with parameters of Table 5., was used for fracture prediction in the numerical simulations of the SPIF.

The feed rate of 6500*mm/s* was used for the forming tool in the FEM simulation for CPU time reduction, but the quasi-static condition of simulation in the Abaqus was investigated by the comparison of the internal and kinetic energies. The ratio of kinetic energy to internal energy should be less than 5 percent for the quasi-static simulations in the Abaqus/Explicit [21]. Comparison of the kinetic and the internal energies has been presented in Fig. 5. As this figure shows, the variation of the kinetic energy is stable and under the internal energy. Therefore, the selected feed rate for the forming tool was used in all FEM simulation of the SPIF.

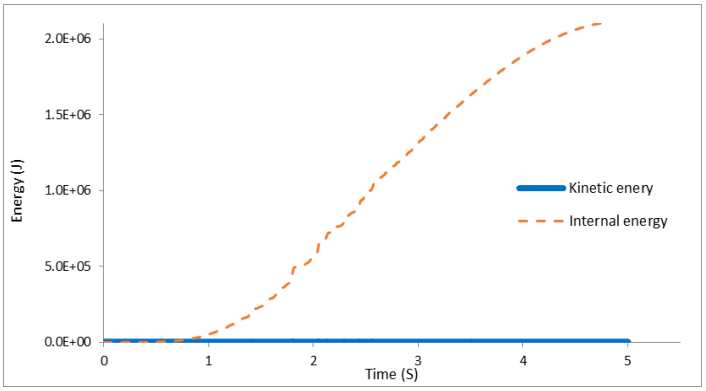

Fig.5
Kinetic and internal energy comparison.

Two sets of experimental tests of the SPIF were done for verification of the numerical model and also the GTN parameters. These experimental tests were done with the process parameters of Table 3. Fig. 6 shows the comparison of the experimental and numerical samples after the SPIF process with two different contact conditions between the forming tool and the blank. Fig. 6 (a) shows the numerical and experimental samples with the frictionless condition were obtained by using oil as a lubricant between the forming tool and the blank in the experimental tests. The penalty contact with frictionless formulation was used in the Abaqus/Explicit. Fracture didn't happen for both numerical and experimental samples in the frictionless condition. As Fig. 6 (a) illustrates the maximum value of VVF is 0.109922 for the numerical sample which is far from $f_f = 0.32$. Fig. 6 (b) shows the comparison of the experimental and the numerical samples after the SPIF in the friction condition. For both

numerical and experimental samples fracture happened in the samples wall near the top corner. In the numerical sample, the VVF = $f_f = 0.32$ at fracture time (Fig. 6 (b)). For better comparison of thinning of the experimental and numerical samples, the thickness variation of both samples in the frictionless condition was extracted along a path across the samples. This path was selected in the region with minimum thickness (Fig. 7). The thickness variation of the FEM and the experimental samples has been presented in Fig. 8. As this figure shows, the thickness variation of the FEM has a good agreement with the experimental results. This figure also shows that the minimum thickness happens in the samples wall near the bottom corner. Fig. 9 shows the forming height comparison of the numerical and experimental samples for two different contact conditions of the forming tool and the blank. In the frictionless and friction condition, the forming height was predicted by the FEM with error values of 0.83% and 3.62%, respectively. These error values showed that the numerical model had good accuracy for the forming height prediction.

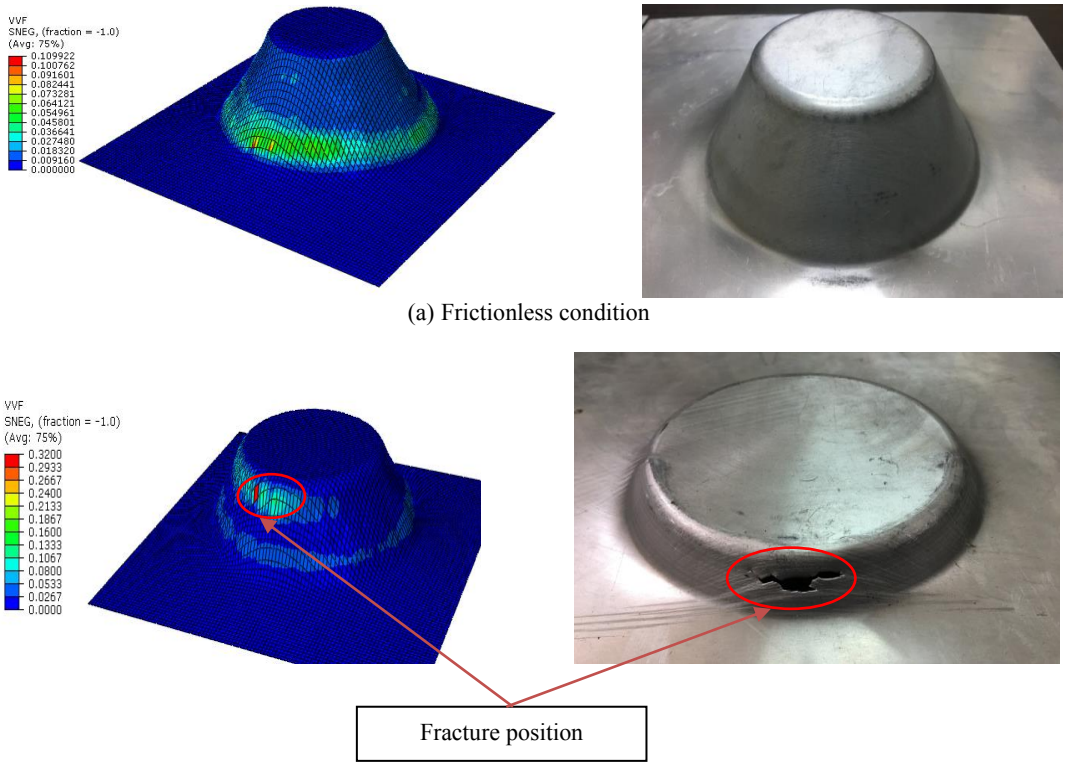

Fig.6
Comparison of experimental and numerical samples after the SPIF.

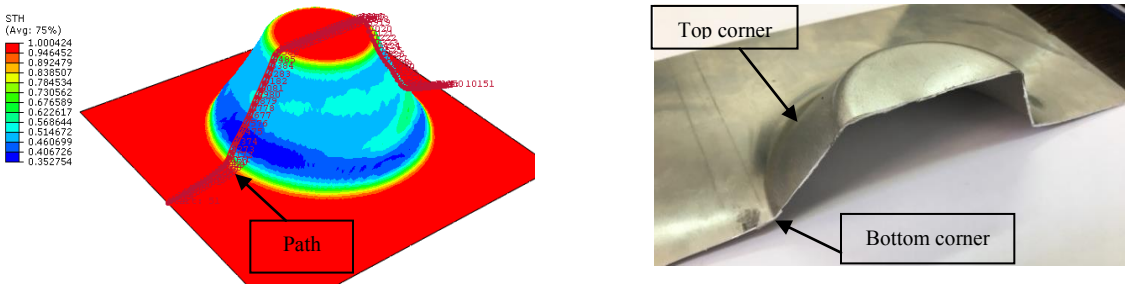

Fig.7
Thickness measuring along a path in the numerical and experimental samples.

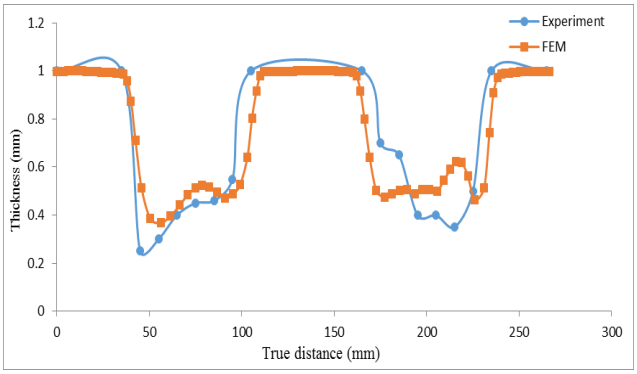

Fig.8
Thickness variation comparison for the experimental and numerical samples.

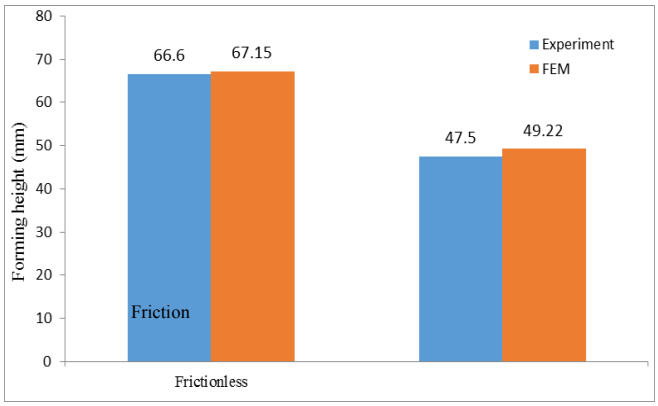

Fig.9
Forming height of the numerical and the experimental samples.

3.3 Effect of the SPIF parameters on the formability
3.3.1 The effect of wall angle of the sample

Four different wall angles of 25°, 30°, 35°, and 45° were selected for the sample in the numerical simulation of the SPIF. The other forming parameters of the SPIF process were constant and were used from the information of Table 3., (verification column). Fig. 10 shows the four samples which formed with the different wall angle. As this figure shows just for the sample with the wall angle of 25˚, the VVF= $f_f = 0.32$ and the fracture happened in the sample's wall near the top corner. The forming height of this sample at fracture time was 27.05 *mm*. For the other three samples, the forming height increased by the wall angle increase. The maximum forming height of 60.33 *mm* happened for the sample with the wall angle of 45˚ at the minimum value of VVF. The effect of wall angle on the thickness variation along a path across the samples has been presented in Fig. 11. As this figure shows, the sample with the wall angle of 25˚ has the lowest level of thickness variation between all samples. The minimum thickness is 0.3 *mm* which happened for the sample with the wall angle of 25˚ and near the top corner, but it is 0.6 *mm* for the sample with the wall angle of 45˚. This figure also shows that the level of thickness variation increase with the wall angle increase. The element with the maximum VVF was selected and the variations of this parameter in the simulation time were compared for all the numerical samples. Fig. 12 shows the effect of wall angle of the samples on the VVF variations. As this figure shows, just for the sample with the wall angle of 25˚ the VVF = $f_f = 0.32$. This figure shows that the VVF decreases with the wall angle increase.

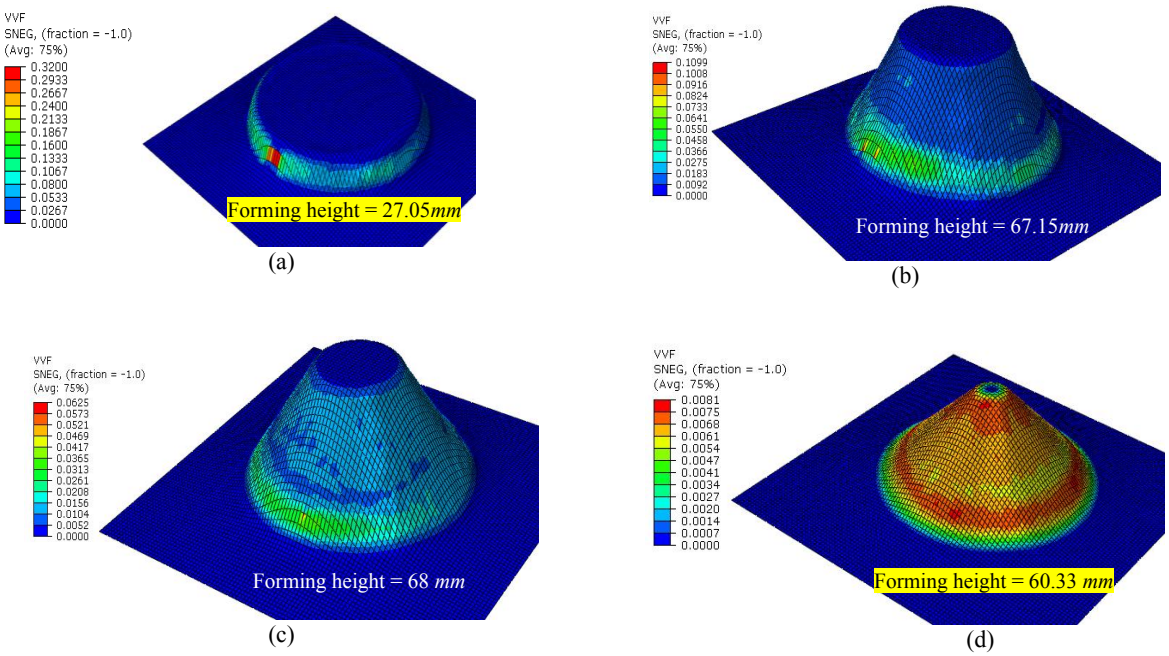

Fig.10
The effect of the sample wall angle of (a) 25˚, (a) 30˚, (a) 35˚and (d) 45˚ on the formability.

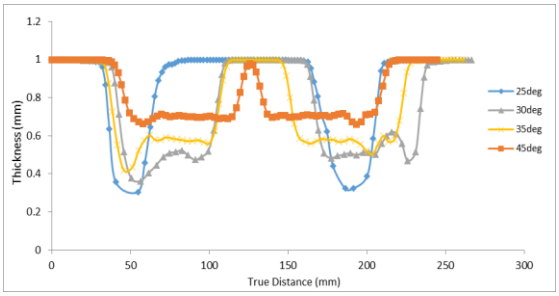

Fig.11
The effect of the wall angle of the sample on the thickness variation across the sample.

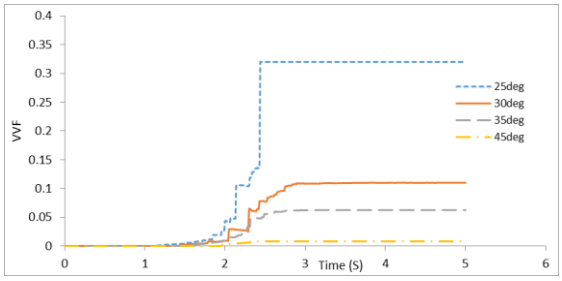

Fig.12
The effect of wall angle of the sample on the VVF variation.

3.3.2 The effect of friction between the forming tool and the blank

In the numerical part of this study, the effect of friction between the tool and the blank was investigated by considering four different friction conditions between the forming tool and the blank. The penalty method was used to model the contact between the forming tool and the blank. These friction conditions were frictionless, penalty contact with the friction coefficient of 0.2, 0.4 and 0.8. The other forming parameters of the SPIF process were selected from the information of Table 3 (verification column). Fig. 13 shows the effect of friction between the forming tool and the blank on the forming height. As this figure shows, the forming height decreases by the increase of friction coefficient from 0.2 to 0.8. Fig. 14 shows the effect of different friction conditions on the thickness variations of the element with the maximum thinning for all the numerical samples. For two samples which formed

in the frictionless and friction with the coefficient of 0.2, the minimum thickness was 0.33 *mm* and 0.29 *mm*, respectively. For two other samples which fractured in the SPIF process, the minimum thickness was 0.24 *mm*. Fig. 15 shows the friction conditions effect on the VVF variations. As this figure shows, for two samples with the friction coefficient of 0.4 and 0.8 the fracture happens when the VVF = 0.32. Therefore, for the SPIF of AA 1050 with presented forming parameters, the friction coefficient in the blank and tool contact should be less than 0.2.

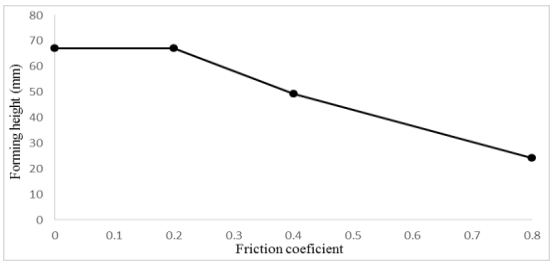

Fig.13
The effect of friction between the blank and the tool on the forming height.

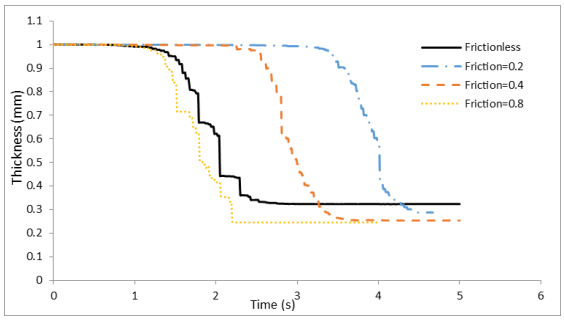

Fig.14
The effect of friction between the tool and the blank on the thickness variation.

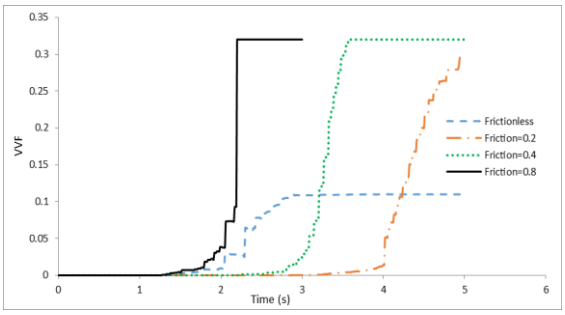

Fig.15
The effect of friction between the tool and blank on the VVF variation.

3.3.3 The effect of forming tool diameter

The forming tool in the SPIF process was a cylindrical rod with a hemispherical head. The effect of tool diameter was investigated by considering four different diameters of 12 *mm*, 14 *mm*, 16 *mm* and 18 *mm*. Fig. 16 shows the effect of tool diameter on the forming height of AA 1050 blanks in the SPIF process. As this figure shows, the forming height is fix (67*mm*) by the tool diameter increase from 12mm to 16mm, but it decreases by the tool diameter increase to 18*mm*.

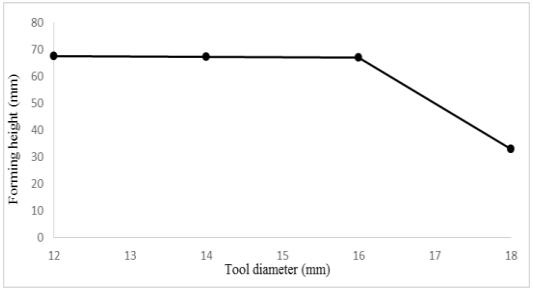

Fig.16
The tool diameter effect on the forming height.

The effect of tool diameter on the thickness variation of the element with the maximum thinning has been presented in Fig. 17 for different tool diameters. As this figure shows, the minimum thickness increases by the increase of tool diameter from 12*mm* to 14*mm*, but it decreases by the tool diameter increase from 14*mm* to 18*mm*. This phenomenon can be explained by this fact that forming pressure increases in the contact area of the tool and the blank by the tool diameter decrease and the thickness decreases in this region. By tool diameter increasing from 14 *mm* to 18 *mm* the contact area increases between the tool and the blank. The tension and shear stress in the sheet and tool contact area increases because of the frictionless condition in the tool and blank contact and causes more deformation in the contact region. Therefore, the thinning increases by the tool diameter increase. Fig. 18 shows the effect of tool diameter on the VVF variation of the critical elements in the samples which were formed with different tool diameters. This figure shows that the VVF = $f_f = 0.32$ for tool diameter of 18 *mm* and this sample was fractured in the forming height of 33.08 *mm*. The sample which formed using the tool with a diameter of 14 *mm* had the minimum value of the VVF and the best formability condition. Because of the frictionless condition, the contact region of the blank with the tool has more deformation compared to other regions of the blank. This deformation increased by the tool diameter increasing and finally the fracture happened for the sample which was formed with a tool diameter of 18 *mm*.

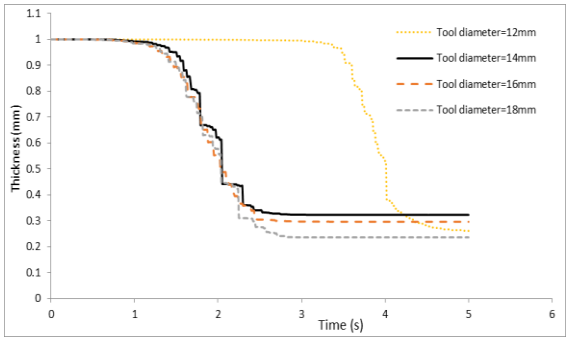

Fig.17
The effect of tool diameter on the thickness variation.

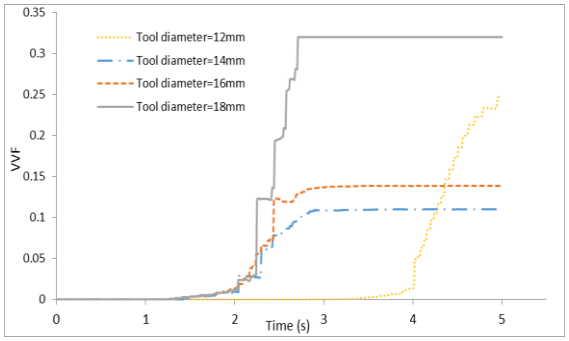

Fig.18
The effect of tool diameter on the VVF variation.

3.3.4 The effect of tool rotation speed

Tool rotation speed is one of the parameters of the SPIF process whose effect was investigated on the formability of samples. For this purpose, four different tool rotation speeds of 100, 250, 500 and 1000 rpm were considered for the forming tool. The other forming parameters were constant and selected from Table 3., (verification column). The contact of the forming tool and the blank was considered frictionless. The effect of tool rotation speed on the thickness variation of the critical elements has been shown in Fig. 19. As this figure shows, using the rotation speed of 250*rpm* and 1000*rpm* causes the minimum thickness of 0.32*mm* and 0.27*mm*, respectively. Fig. 20 shows the effect of tool rotation speed on the VVF variations. This figure shows that for all samples the value of VVF didn't reach to the $f_f = 0.32$ and samples were formed without any fracture, but two samples which formed with the rotation speed of 250 *rpm* and 500 *rpm* had the better condition of formability and thinning.

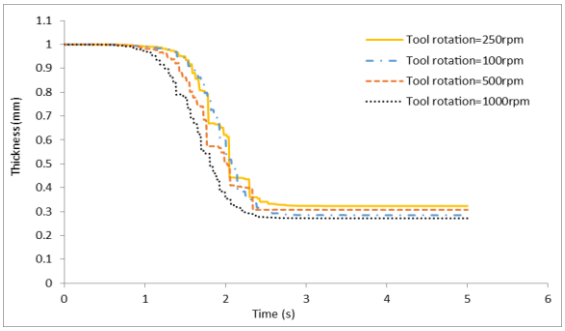

Fig.19
The effect of tool rotation speed on the thickness variation.

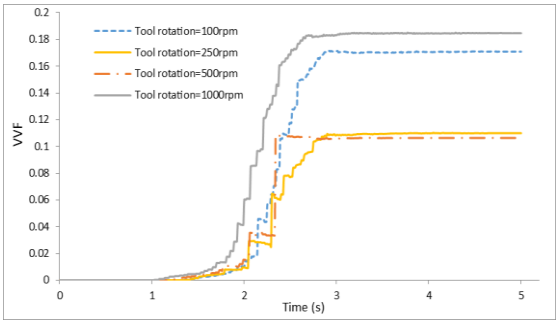

Fig.20
The effect of tool rotation speed on the VVF variation.

3.3.5 The effect of tool travel speed (feed rate)

Whereas the numerical simulation of the sheet metal forming process should be done in the quasi-static condition in the Abaqus/Explicit [21], this condition should be considered in the selection of the forming speed (feed rate in the SPIF process). The ratio of kinetic energy to internal energy should be less than 5 percent for the quasi-static simulation [21]. Therefore, in the present study, three different feed rates of 6500 *mm/s*, 7500 *mm/s* and 8000 *mm/s* were selected by considering the quasi-static condition. The other forming parameters were constant and selected from Table 3. The kinetic and internal energies has been compared in Fig. 5. The effect of feed rate on the thickness variations of critical elements has been compared in Fig. 21. As this figure shows, the sample which was formed with the feed rate of 6500 *mm/s* had the maximum thickness and the thickness decreased by the feed rate increase. Fig. 22 shows the effect of tool feed rate on the VVF variations. The VVF = f_f for the sample which was formed using the feed rate of 8000 *mm/s* and it fractured at the forming height of 49.61 *mm*. For two other samples, the value of VVF was less than $f_f = 0.32$ and fracture didn't happen in these samples. The sample which was formed with the feed rate of 6500 *mm/s* had the minimum level of the VVF.

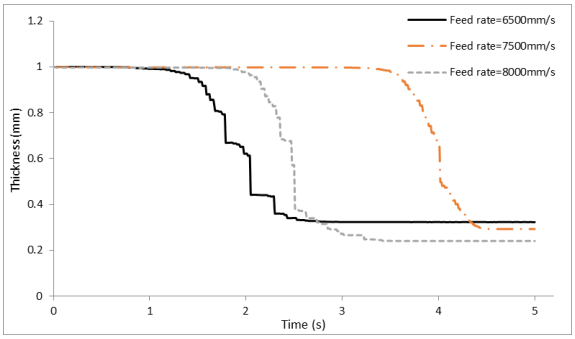

Fig.21
The effect of tool feed rate on the thickness variation.

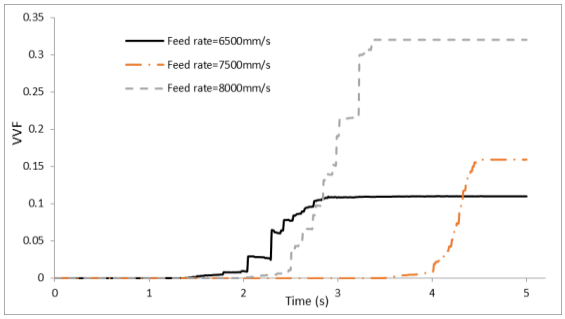

Fig.22
The effect of tool feed rate on the VVF variation.

3.3.6 The effect of vertical pitch

The effect of the vertical pitch was investigated on the formability of AA 1050 blank in the SPIF by considering four values of 0.6 *mm*, 1.2 *mm*, 2 *mm* and 3.5 *mm* for it. The other forming parameters were constant and selected from Table 3., (verification column). The frictionless condition was used in the contact of the forming tool and the blank. Fig. 23 shows the effect of vertical pitch on the thickness variation of the critical element. As this figure shows, the sample which was formed with the vertical pitch of 1.2 *mm* had the maximum thickness. The effect of vertical pitch variation on the VVF has been shown in Fig. 24. Therefore, the formability and the forming height increased by the vertical pitch increase from 0.6 *mm* to 1.2 *mm*. Hirt et al. [22] also resulted that the formability of the SPIF process improved by the increase of vertical pitch. Whereas the tensile stress increases in the sample wall with the vertical pitch increase, the forming height decreases by the vertical pitch increase from 1.2 *mm* to 3.5 *mm*. Therefore, the best value for the vertical pitch was 1.2 *mm*.

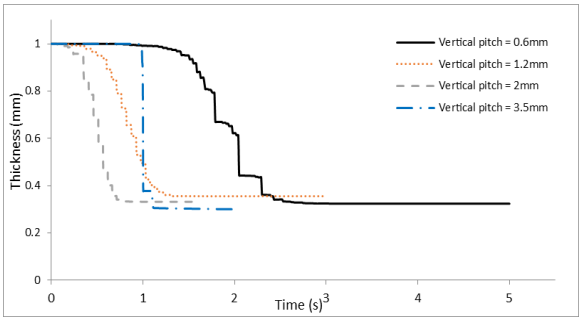

Fig.23
The effect of vertical pitch on the thickness variation.

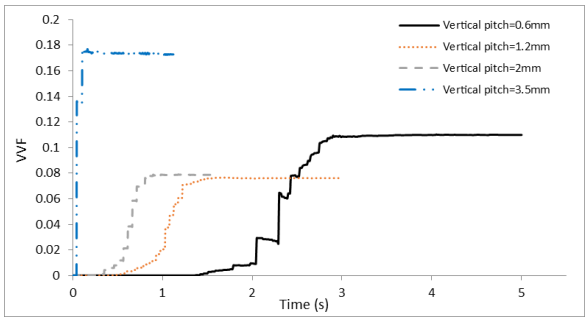

Fig.24
The effect of vertical pitch on the VVF variation.

4 CONCLUSIONS

In the present study, the GTN damage model was used for fracture prediction of AA 1050 sheet in the SPIF process. Design of experiment coupled with the numerical simulation of the uniaxial tensile test in the Abaqus/Explicit to identify the parameters of the GTN damage model using the anti-inference method. The effect of GTN parameters was investigated on the stress-strain curve of the numerical tensile test. Results indicated that the numerical stress-

strain curve was more sensitive to the ε_N , f_N and variations of two other parameters of f_f and f_c didn't have a significant influence on it.

The identified parameters were used in the numerical simulation of the SPIF process to produce a truncated cone. The numerical results were compared with the experimental results for two different contact conditions of frictionless (using oil as a lubricant) and dry contact between the tool and the blank. Results showed that there was a good agreement between the numerical and the experimental results. The GTN damage model had good accuracy for prediction of fracture position and the forming height.

The effects of main parameters of the SPIF were investigated on the formability, fracture position, thickness variation, forming height and the VVF variations by the verified numerical model. The results indicated that the formability and the forming height increased by the increase of the sample wall angle and fracture happened in the sample with the wall angle of 25˚. The formability and the forming height decreased by the increase of the tool feed rate and the friction coefficient in the forming tool and the blank contact. The best parameters were the frictionless contact and the feed rate of 6500 *mm/s*. Results showed that the tool rotation speed didn't have a significant influence on the formability of AA1050 in the SPIF. The samples' formability increased by the tool diameter increase from 12 *mm* to 14 *mm* and decreased by increasing from 14 *mm* to 18 *mm*. Results indicated that the forming height increased by the vertical pitch increasing from 0.6 *mm* to 1.2 *mm* and it was vice versa by increasing from 1.2 *mm* to 3.5 *mm*. Therefore, the tool diameter of 14 *mm* and the vertical pitch of 1.2 *mm* were the best parameters for the SPIF of AA 1050.

REFERENCES

[1] Bagudanch I., Garcia-Romeu M.L., Ferrer I., Lupiañez J., 2013, The effect of process parameters on the energy consumption in single point incremental forming, *Procedia Engineering* **63**: 346-353.

[2] Gatea S., Ou H., McCartney G., 2016, Review on the influence of process parameters in incremental sheet forming, *The International Journal of Advanced Manufacturing Technology* **87**(1): 479-499.

[3] Raju C., Haloi N., Sathiya Narayanan C., 2017, Strain distribution and failure mode in single point incremental forming (SPIF) of multiple commercially pure aluminum sheets, *Journal of Manufacturing Processes* **30**: 328-335.

[4] Guzmán C.F., Yuan S., Duchêne L., Saavedra Flores E.I., Habraken A.M., 2018, Damage prediction in single point incremental forming using an extended Gurson model, *International Journal of Solids and Structures* **151**: 45-56.

[5] Dakhli M., Boulila A., Tourki Z., 2017, Effect of generatrix profile on single-point incremental forming parameters,*The International Journal of Advanced Manufacturing Technology* **93**(5): 2505-2516.

[6] McAnulty T., Jeswiet J., Doolan M., Formability in single point incremental forming: A comparative analysis of the state of the art, *CIRP Journal of Manufacturing Science and Technology* **16**: 43-54.

[7] Bagudanch I., Centeno G., Vallellano C., Garcia-Romeu M.L., 2013, Forming force in single point incremental forming under different bending conditions, *Procedia Engineering* **63**: 354-360.

[8] Palumbo G., Brandizzi M., 2012, Experimental investigations on the single point incremental forming of a titanium alloy component combining static heating with high tool rotation speed, *Materials & Design* **40**: 43-51.

[9] Hadoush A., van den Boogaard A.H., 2009, Substructuring in the implicit simulation of single point incremental sheet forming, *International Journal of Material Forming* **2**(3): 181-189.

[10] Duflou J.R., Verbert J., Belkassem B., Gu J., Sol H., Henrard C., Habraken A.M., Process window enhancement for single point incremental forming through multi-step toolpaths, *CIRP Annals* **57**(1): 253-256.

[11] Gupta P., Jeswiet J., 2017, Observations on heat generated in single point incremental forming, *Procedia Engineering* **183**:161-167.

[12] Edwards W.L., Grimm T.J., Ragai I., Roth J.T., Optimum process parameters for springback reduction of single point incrementally formed polycarbonate, *Procedia Manufacturing* **10**: 329-338.

[13] Bansal A., Lingam R., Yadav S.K., Venkata Reddy N., 2017, Prediction of forming forces in single point incremental forming, *Journal of Manufacturing Processes* **28**: 486-493.

[14] Behera A.K., de Sousa R.A., Ingarao G., Oleksik V., 2017, Single point incremental forming: An assessment of the progress and technology trends from 2005 to 2015, *Journal of Manufacturing Processes* **27**: 37-62.

[15] Martins P.A.F., Bay N., Skjoedt M., Silva M.B., 2008, Theory of single point incremental forming, *CIRP Annals* **57**(1): 247-252.

[16] Martínez-Romero O., García-Romeu M.L., Olvera-Trejo D., Bagudanch I., Elías-Zúñiga A., 2014, Tool dynamics during single point incremental forming process, *Procedia Engineering* **81**: 2286-2291.

[17] *(ASTM) ASfTaM, Metals Test Methods and Analytical Procedures*, **1999**: 78-98, 501-508.

[18] Chu C.C., Needleman A., 1980, Void nucleation effects in biaxially stretched sheets, *Journal of Engineering Materials and Technology* **102**(3): 249-256.

[19] He M., Li F., Wang Z., 2011, Forming limit stress diagram prediction of aluminum alloy 5052 based on GTN model parameters determined by in situ tensile test, *Chinese Journal of Aeronautics* **24**(3): 378-386.

[20] Kacem A., Jégat A., Krichen A., Manach P.Y., 2013, Forming limits in the hole-flanging process by coupled and uncoupled damage models, *AIP Conference Proceedings* **1567**(1): 575-578.
[21] Hibbitt K., Sorensen, 2002, ABAQUS/CAE User's Manual, Incorporated.
[22] Hirt G., Ames J., Bambach M., Kopp R., 2004, Forming strategies and process modelling for CNC incremental sheet forming, *CIRP Annals* **53**(1): 203-206.